Spatiotemporal Modeling of Laser Tissue Soldering Using Photothermal Nanocomposites

Madaline Mushaben[1,#], **Russell Urie**[2,#], **Tanner Flake**[2], **Michael Jaffe**[3], **Kaushal Rege**[2], and **Jeffrey Heys**[1,*]

[1]Chemical and Biological Engineering, Montana State University, Bozeman, MT

[2]Chemical Engineering, Arizona State University, Tempe, AZ

[3]College of Veterinary Medicine, Midwestern University, Glendale AZ 85308

Abstract

Objective—Laser tissue soldering using photothermal solders is a technology that facilitates rapid sealing using heat-induced changes in the tissue and the solder material. The solder material is made of gold nanorods embedded in a protein matrix patch that can be placed over the tissue rupture site and heated with a laser. Although laser tissue soldering is an attractive approach for surgical repair, potential photothermal damage can limit the success of this approach. Development of predictive mathematical models of photothermal effects including cell death, can lead to more efficient approaches in laser-based tissue repair.

Methods—We describe an experimental and modeling investigation into photothermal solder patches for sealing porcine and mouse cadaver intestine sections using near-infrared laser irradiation. Spatiotemporal changes in temperature were determined at the surface as well as various depths below the patch. A mathematical model, based on the finite element method, predicts the spatiotemporal temperature distribution in the patch and surrounding tissue, as well as concomitant cell death in the tissue is described.

Results—For both the porcine and mouse intestine systems, the model predicts temperatures that are quantitatively similar to the experimental measurements with the model predictions of temperature increase often being within a just a few degrees of experimental measurements.

Conclusion—This mathematical model can be employed to identify optimal conditions for minimizing healthy cell death while still achieving a strong seal of the ruptured tissue using laser soldering.

Keywords

laser tissue solder; heat transfer; cell death; gold nanorods; finite elements

---

[*]To whom all correspondence is to be addressed: Prof. Jeffrey Heys, Department of Chemical and Biological Engineering, 306 Cobleigh Hall, Montana State University, Bozeman, MT 59717-3920, USA.
[#]equal contribution

Introduction

Sutures are a ubiquitous part of surgery, with approximately 90 million surgical incisions requiring closure each year in the U.S. and 3 million stitches placed daily around the world [1]. Sutures and staples, however, do not provide an immediate seal to the tissue and, additionally, cannot functionally repair tissues in some cases [2]. The ability to rapidly seal ruptured or incised tissue has the potential to decrease infection, leakage, reduced scarring, and healing time compared to suturing [3–5]. Tissue sealants, adhesives, and glues have thus far been limited in their application and ability to rapidly seal tissue reproducibly, especially when bearing a load [6,7]. Surgical glues have wide use in topical applications, but, due to long polymerization times and toxicity concerns, glues have seen very limited internal use, especially in wet wound environments [8]. Recently developed nanoparticle solutions have been shown to provide rapid adhesion between two hydrogels. The method relies on the nanoparticle adsorbing onto polymer gels to connect the polymer chains [9,10].

Alternatively, laser tissue soldering (LTS) is a rapid tissue sealing technique in which a chromophore converts laser light to heat. This heat induces structural changes in the native tissue and/or biomaterial "solder" leading to a tissue seal through photocoagulation and protein interdigitation (Figure 1) [11–14]. The laser-absorbing chromophore may be a native tissue constituent or an exogenous material injected or applied to the surgery site. Native chromophores, including water, melanin, and hemoglobin [15] are present in significant amounts within tissues, and have the advantage of eliciting no foreign body response. However, efficient light absorption by these chromophores prevents deep laser penetration which, in turn, can lead to extensive superficial heating but limited heating in deep tissues [16]. Endogenous chromophores have therefore been extensively studied in thin, transparent, and homogenous tissue, but have been minimally effective in sealing larger tissue geometries [17].

To overcome these challenges, exogenous chromophore formulations have been used as stains [17–19], pastes [12], or patches [3,20] in concert with lasers tuned to near infrared wavelengths, at which laser absorbance in the tissue is higher compared to light at visible wavelengths. Tissue stains using aqueous solutions of the organic dye indocyanine green (ICG), and tissue solders largely composed of albumin-ICG viscous liquids or semi-solids have been used [21]. These chromophores work effectively at differentiating laser absorbance from that of the tissue, but organic dyes lack long-term stability and often leach to peripheral tissue [22]. Simultaneously, viscous solders have been criticized for difficulty with reproducing robust soldering with consistency [2,23,24].

Plasmonic nanoparticles, including gold nanorods, are inert and stable, easily modified, and convert laser light to heat approximately a million-fold more effectively than organic dyes [25], although there are some cytotoxity and bio-elimination concerns [26,27]. The LTS approach of interest here is based on nanocomposite solders composed of gold nanorods (GNRs) cross-linked or embedded within a polypeptide matrix. In the former case, elastin-like polypeptides (ELP) were crosslinked with GNRs, resulting in the formation of thin film patches [3], and, in the latter case, collagen hydrogels were physically embedded within GNRs and compressed plastically to form thin film hydrogel patches [20]. ELP-GNR

nanocomposites successfully soldered *ex vivo* porcine intestine in a 47% return in tensile strength and a 45% return in burst pressure compared to intact intestine, and collagen-GNR nanocomposites similarly resulted in a 68% return in tensile strength and a 42% return in burst pressure compared to intact intestine. The extent of laser absorption in these nanocomposites depends on the wavelength of the laser and the absorbance of the chromophore.

Gold nanorods tuned to a maximum absorbance at 800 nm were selected because light is minimally absorbed by water and tissue constituents in the therapeutic window [28]. In this work, collagen-GNR nanocomposite hydrogels are used in conjunction with 800 nm NIR laser to solder ruptured porcine intestine.

In addition to tensile strength and burst pressure, the temperature reached during soldering is paramount in establishing the integrity of the solder [29] while also mitigating tissue damage. Thermal denaturation of collagenous tissue is proposed to follow a three-step mechanism [30–32], which illustrates the temperature range necessary for forming new tissue bonds. First, at approximately 45°C, interfibrillar bridges are broken and the parallel collagen fibril arrangement is impaired. Second, around 60°C intramolecular hydrogen bonds are broken, and the fibrillar edges are frayed. Finally, at 80°C, the covalent bonds within and between collagen molecules are broken, leading to full denaturation, and the tissue becomes homogenized. From this proposed mechanism and previous studies in laser tissue soldering, it has been seen that the optimal temperature window for tissue bonding is between 60–67°C [33,34]. However, healthy, living cells heated to these same temperatures are likely to be injured or killed by hyperthermia [35]. One promising approach for minimizing healthy cell damage by hyperthermia is the development of micro-particles containing GNRs and superparamagnetic particles agglomerated in a layered polyelectrolyte multilayer matrix. Magnetic particle guidance can be used to enrich the particles in the tissue incision for wound sealing, and the results show damaged areas of less than 100 microns of tissue [36,37].

The development of a spatiotemporal model of heat transfer and cell death is motivated by the goal of identifying the optimal conditions for performing laser tissue soldering to help mitigate damage to nearby healthy cells while maximizing solder integrity. A mathematical model of heat transfer and cell death proximal to the nanocomposite and in nearby tissue is described here with the objective of accelerating the identification of optimal LTS treatment parameters. Effective integration of mathematical modeling with laser solder operation can potentially reduce the overall number and duration of experimental trials and potentially lead to improved outcomes for tissue repair by minimizing healthy tissue damage. Most mathematical modeling of laser-tissue interactions has focused on the heating and coagulation of tissue, not the fusing of tissue, and has not included an exogenous chromophore or solder material. Model predictions of tissue temperatures are important because it is difficult to measure the temperatures reached below the treatment surface during LTS, especially in larger tissue geometries where LTS has had less success. The model is validated using porcine intestine and murine colon experimental results.

Methods

Nanocomposite Synthesis

Collagen-gold nanorod (GNR) nanocomposites were generated based on methods previously described by us [3,28,29,38]. Briefly, gold nanorods (GNRs) with a maximum absorbance at 800 nm were synthesized using the Nikoobakht seed-mediated method [39]. GNRs were then centrifuged repeatedly and redispersed in nanopure (de-ionized) water to a final cetyltrimethylammonium bromide (CTAB) concentration below 0.25mM. Nanorods were dispersed in 4 mg/mL rat tail type 1 collagen at a concentration of 5 wt% GNRs. These collagen-GNR dispersion solutions were brought to neutral pH while on ice and aliquoted into a 48-well plate (12 mm diameter wells). The well plate was kept at 30°C for 1–3 hours to allow the collagen solutions to gel. The resultant gels were roughly 10 mm in height. A hollow cylindrical weight filled with absorbent tissue paper was use to compress the gels and remove excess liquid until the gels were < 1 mm in thickness.

Laser Configuration

A titanium sapphire laser pumped by a solid-state laser (Spectra-Physics, Millennia) was configured in the following manner: a 2 mm-diameter beam was passed through a cylindrical lens, and the subsequent laser light was screened by small mask with an approximately 0.5 mm $\times$ 3 mm opening to adjust the area of exposure to 2 mm $\times$ 15 mm at the focus length to simultaneously irradiate the entire portion of the nanocomposite patch covering the wound site (~30 mm^2 area). The laser was tuned to match the maximum absorbance of the collagen-GNR nanocomposites, i.e. 800 nm.

Laser Soldering of Porcine Intestinal Tissue

The effectiveness of the laser tissue solder has been previously demonstrated through measuring the tissue burst pressure and tensile strength after soldering. Intestinal porcine tissue was defrosted in water and kept moist at $20°C$. First, a 1-cm long incision is made through one wall (~2mm thick) of a section of intestine at the tissue center. The tissue was laid flat on a plastic surface, the incision edges were approximated, and a nanocomposite was placed over the incision [3]. An infrared (IR) camera (ThermaCAM PS60 from FLIR) was placed directly above the tissue and nanocomposite configuration to capture top-down IR images for recording a 2D array of surface temperatures. The center of the nanocomposite corresponding to the incision area was then irradiated at power densities from 0.83 to 2.33 W/cm^2 for up to 8 minutes. IR images were recorded every 5 seconds during the laser irradiation. Additionally, a Digi-Sense J-type thermocouple (~1.75 mm diameter fiber) was placed directly below the tissue under the center of the nanocomposite. The thermocouple temperature was recorded every 15 seconds. It should be noted that the temperature of an individual nanoparticles is higher than the regional thermocouple temperature measurements reported here [40–43].

To compare wound patency, the section of sealed intestine was clamped at both ends and infused with a dyed saline solution until bursting, measuring the maximum internal pressure to determine how much of the native tissue strength was recovered by soldering. A DPI 795 digital manometer (Druck) was placed in parallel to the flow of the dyed saline. Using this

manometer, pressure within the intestinal sample was measured. Burst pressure was defined as the point at which the maximum pressure was reached. The change in pressure from the initiation of the experiment to the bursting point was recorded. A syringe pump (NE 300, New Era Pump Systems, Inc) first purged the line and hypodermic needle (26 gauge) for roughly 1 minute, at which point the pressure in the system was constant and was zeroed using the manometer prior to the infusion line and needle being inserted into the intestine. The intestine section was clamped at both ends and filled with saline solution dyed with green food coloring at a flow rate of 0.5 mL/min using the syringe pump. The infusion continued until intestinal rupture.

The strength of the solder was also tested using rectangular slabs of approximately 50 mm length and 15 mm width of tissue with a soldered incision that was clamped at each end, and an increasing force was applied using a TA.XT Plus Texture Analyzer (Texture Technology Corp.) until failure, extended at a rate of 1 mm/s in uniaxial tension. This force on the tissue under tension was measured using the accompanying Exponent software (Stable Microsystems) to determine the ultimate tensile strength of the tissue by taking the maximum force normalized by cross-sectional area of the tissue being tested.

Laser Soldering of Intestinal Tissue in Mouse Cadavers

Freshly euthanized C57BL/6 mouse cadavers were also used for evaluation of laser tissue soldering. A midline incision was made in each cadaver, and the colon was unpacked from the body cavity. The colon was folded over twice, as shown in Figure 2. While exact dimensions of the mouse colon are difficult to measure, the mouse colon is assumed to be approximately 0.5 mm thick, as shown in Figure 2. The nanocomposite patch was partly wrapped around the colon. Similar to the porcine intestine, the IR camera was placed directly above the tissue-nanocomposite configuration to record surface temperature data during laser irradiation; however, unlike the porcine intestine, the thermocouple was arranged in one of three configurations, as shown in Figure 2. In one configuration, the thermocouple was inserted into the lumen of the primary section of colon tissue with internal contact on both intestinal walls, and temperatures were recorded. In a second configuration, the thermocouple was inserted in between the primary and secondary colon tissue sections and in direct contact with both. In the final configuration, the thermocouple was inserted in the lumen of the secondary tissue similar to configuration one. In each configuration, the thermocouple was located directly below the nanocomposite that was being irradiated by the laser.

Mathematical Model

Heat Transfer

A modified form of the Pennes Bio-heat Equation was used to model heat transfer in laser tissue soldering simulations. This equation is used to model the heat transfer within tissues, including in tissues with blood flow [44,45]. Equation 1 consists of the simplified form of this equation used in the nanocomposite model:

$$\frac{dT}{dt} = \alpha \nabla^2 T + \frac{Q_{laser}}{C_p \cdot \rho}(1 - 10^{-OD}).$$

(1)

The first term of Equation 1 accounts for thermal diffusion, where α is thermal diffusivity of both the tissue and the nanocomposite patch and is defined by Equation 2:

$$\alpha = \frac{k}{C_p \cdot \rho}$$

(2)

where k is the thermal conductivity of the nanocomposite patch or surrounding tissue, C_p is the heat capacity for both the nanocomposite patch and the tissue, and ρ is the density. The second term in Equation 1 accounts for the heat generation from the laser energy absorbed by the GNR-infused collagen patch. The variable Q_{laser} refers to the laser power density for the system, and OD is the optical density of the nanocomposite patch. An additional term accounting for blood flow was excluded here due to the lack of blood flow in the experimental system that was used for model validation, and while blood flow has been shown to have a heat-sinking effect, the blood vessels would be coagulated so quickly that the effect of blood flow is minimal [46]. The equation was transformed into a time-dependent, variational problem and approximately solved on the domains of interest using the finite element method.

The tissue surrounding the patch was assumed to initially be at a fixed temperature, and the modeled tissue region extended sufficiently far beyond the nanocomposite patch such that fixed temperature (i.e., Dirichlet) boundary conditions were applied to the four exterior sidewalls of the porcine model domain and the two end walls of the mouse model domain. This assumption was validated two ways: first, the magnitude of the temperature gradient near the wall was checked (a gradient of less than $1°C/mm$ was observed) and the size of the domain was increased to confirm that the temperature in the region of interest did not change significantly. A no-flux boundary condition was applied along the bottom tissue surface to represent the low thermal conductivity surface used for the porcine experimental measurements, and a fixed temperature boundary condition was used along the bottom tissue surface to reflect the additional intestinal tissue present in the mouse experiments. A Robin boundary condition was applied along the top of the nanocomposite surface that is exposed to air. The Robin boundary condition, which accounts for convection occurring at the air-composite interface, was applied along the upper surface using:

$$\frac{\partial T}{\partial n} = \frac{U_{air}}{k}(T - T_o)$$

(3)

where U_{air} is the overall heat transfer coefficient for air, T is the local tissue/nanocomposite surface temperature (changing with time), and T_0 is the bulk air temperature.

The model parameters for the nanocomposite patch system are listed in Table 1. Many of the parameters were based on values determined previously for an *in vitro* GNR and cell system [28], and many parameter values are relatively close to those of water, consistent with the high water content of the nanocomposite patch and intestinal tissue.

In the LTS experiments, the cylindrical intestine was relaxed into a relatively flat, rectangular shape that was the thickness of the pair of intestine walls, and the width was roughly half the circumference of the intestine. As a result of this configuration, the geometry used in the model of the porcine intestinal tissue was a 3-dimensional rectangular domain with dimensions of [50 mm × 20 mm × 4 mm], divided into a tetrahedral finite element mesh with divisions of [100 × 40 × 20] for the rectangular, 3-dimensional domain. Simulations were also run on a higher resolution finite element mesh ([150 × 60 × 30] divisions) to confirm that the temperature solution changed by less than 2%. A cylindrical patch, 10 mm in diameter and approximately 1 mm in height, was added atop the tissue surface to represent the nanocomposite solder material. The temperature prediction comparison of the finer meshes to the primary mesh deviated by less than 2%. A diagram depicting the full model domain (intestinal tissue and nanocomposite patch) with the corresponding boundary conditions is displayed in Figure 3.

Cell Death Prediction

The Arrhenius cell injury model was used to predict cell death and injury within the tissue [49,50]. Applying the Arrhenius equation (Equation 4), the rate of cell injury can be calculated as:

$$k = A e^{-\frac{E_a}{R \cdot T}} \quad (4)$$

where A is a scaling factor, E_a is the activation energy for injury of the cell, R is the universal gas constant, and T is the local temperature. The variables A and E_a were estimated based on previous cell death measurements in a human cell line (PC3-PSMA), and their corresponding values are included in Table 1 [28]. These values were also found to be consistent with the values measured for cells and tissue of similar nature [51,52]. The fraction of cells killed, F_D, was calculated by integrating the accumulated cell injury, k, using Equation 5 [28].

$$F_D = 1 - e^{\int_0^t k * dt} \quad (5)$$

The values for F_D range from 0 to 1, with values closer to 1 approaching 100% cell death prediction.

Mouse Cadaver Model

A model similar to the porcine model was created to predict spatiotemporal temperature profiles and corresponding cell death in the intestinal tissue of mice using many of the same

parameters. Variations in the parameters were limited to dimensions of the tissue and laser power density. The mouse model domain had the same shape as the porcine model (i.e., a flattened intestine), but the dimensions for the mouse model were 20 mm × 10 mm × 4 mm. Although the wall thickness of the mice intestinal tissue is less than 1 mm, multiple layers of intestinal tissue were present so the overall tissue thickness was set to 4 mm in the z-direction, and the 20 mm length was chosen to ensure that the fixed temperature boundary condition was valid. The laser power density used in this experiment was $0.0167 \frac{W}{mm^2}$, resulting in an overall laser power per volume of $9.67 \frac{W}{mm^3}$ for the nanocomposite patch. A thermocouple was placed in three different locations within the tissue sample: inside the upper segment of intestine, between the upper and lower segments, and inside the lower segment of intestine (Figure 2).

Results and Discussion

Porcine Cadaver Intestine Model

The heat transfer model was used to predict the temperature distribution within the nanocomposite and porcine intestine. The maximum surface temperature was predicted to reach a value of 69°C (Figure 4A) after 4 minutes of laser irradiation at 2.33 W/cm^2 CW, which was consistent with experimental measurements (67°C, Figure 5). Due to the elliptical nature of the laser, this elevated temperature at the patch surface extended outward from the center 10 mm by 2 mm ellipse in the x- and y-directions, respectively, in both the IR images acquired during experimentation and in model predictions as shown in Figure 4. The temperature decreased as the distance from the center of the area of laser exposure in the nanocomposite increased, with the outermost diameter of the patch attaining a temperature of approximately 45°C. Outside the 10 mm diameter of the patch, the domain has a moderately elevated temperature extending approximately 2 mm and 3 mm in the x- and y-directions, respectively.

The heat transfer model predictions are compared to experimental measurements in Figure 5. The temperature at two different points within the experimental system was monitored during laser irradiation of the nanocomposite at 2.33 W/cm^2 CW for 4 minutes. The first location is the surface temperature at the top of the domain (the nanocomposite surface at the laser exposure center), and the second location is inside of the intestinal lumen, directly below the nanocomposite and the 4 mm thick intestine wall. The individual data points show the experimental measurements at the two different locations, and the solid lines show the heat transfer model prediction of the temperatures at these experimental conditions. Variation within the surface temperatures of the experimental data are seen when incorporating the thermocouple directly underneath in the lumen because the operator holding the thermocouple can create small movements in the LTS configuration. The heat transfer model predictions agree well with the trends shown in experimental data for the nanocomposite and tissue surface temperatures (Figure 5). The agreement is not as good, however, for the temperature inside the intestinal lumen for the earlier time points, which show a difference of approximately 5°C between the heat transfer model prediction and experimental measurements during the first three minutes of the four-minute LTS experiment. In the final minute, the model predictions and experimental results show

significantly better agreement. This difference may be due to potential energy absorption directly by the metal thermocouple below the tissue surface. Exploring a different experimental setup for measuring luminal temperatures may improve the experimental results by removing any artifacts in heat generation.

The profile view of the nanocomposite (Figure 6) displays a predicted temperature gradient extending through the entire depth of both the 1 mm patch and 4 mm tissue. The elevated temperatures (>45°C) extend approximately halfway through the depth of the tissue. These results show that even for extended heating periods (4 min) peripheral tissue surface temperature is predicted to rise very little as close as 3 mm in the x or y direction from the nanocomposite patch. Additionally, the temperatures predicted below the tissue surface do not extend beyond 3 mm in the x or y direction from below the nanocomposite. The temperature within the nanocomposite is above approximately 55°C uniformly throughout the material, although the surface of the nanocomposite is not uniformly exposed to the laser suggesting that the GNRs in the nanocomposite rapidly heat up and transfer heat throughout the nanocomposite. These elevated temperatures extend through the nanocomposite and into the intestinal tissue directly below.

The results of the cell death model predictions in porcine intestine are shown in Figure 7. As temperature and time at the elevated temperature increased, cell death also increased. With temperatures reaching above 50°C for some of the tissue depth, close to 100% of the cells in the portion of the domain where temperatures exceeded 50°C were predicted to have been killed by hyperthermia (Figure 7). It is interesting to note the sharper transitions (i.e., sharper gradients) in the cell death model predictions relative to temperature predictions. Increased cell death at higher temperatures is due to the exponential relationship between hyperthermal cell death and temperature that is described by the Arrhenius cell death model. This result suggests that any cell death that results from the LTS process is likely to be mostly limited to the tissue immediately adjacent to and below the soldering nanocomposite and limited beyond that region. It should be noted, however, that additional, longer-term cell death may occur after the initial thermal insult [53]. In a surgical setting, this region directly below the nanocomposite includes the negative space of the wound bed and the tissue edges likely to become necrotic as the wound heals. The incision space and necrotic tissue negate much of the concern regarding extensive cell death directly underneath the nanocomposite, where the majority of cell death occurs as shown in Figure 7.

Increasing the duration of the laser treatment resulted in higher temperatures and longer time for injury accumulation in both the immediate area undergoing laser irradiation as well as the surrounding area, and these increased temperatures and accumulated injuries are predicted to generate more extensive cell death. For this reason, the power density and duration of laser treatment must be limited to mitigate any extensive and peripheral elevated temperatures and extensive cell death [54]. Ultimately, an optimum set of conditions should exist that balance the increase in temperature with the duration of the heating.

Because exact mechanisms of LTS and heat-induced tissue fusion are not entirely known [55,56], the spatiotemporal model cannot be extended to predict solder integrity at various LTS power densities and laser durations. It has been hypothesized in the literature, however,

that a critical soldering temperature exists below which protein interdigitation [57] and bonding [12] will not occur. General consensus in the field is that the critical temperature is in the range of 60–65°C [18], although this varies by tissue type.

Below this critical temperature, solder strength will be insufficient to cause tissue fusion, while above this temperature, thermal damage increases significantly and tensile strength is decreased [25]. Correlating the temperature to mechanical strength (while exact mechanisms are not known) can aid in determining the critical soldering temperature as well as in adjusting parameters that can be employed to lower the temperature while maintaining solder integrity to further limit thermal damage and cell death. This is demonstrated in Figure 8, which shows that irradiation of the nanocomposite using a laser at 1.83 W/cm^2 for four minutes results in a steady-state temperature of approximately 57°C after roughly 4 minutes (white boxes), and at 2.33 W/cm^2 results in approximately 75°C in 4 minutes (black boxes). Additionally, a negligible rise in temperature is seen for collagen films in absence of GNRs following irradiation with NIR laser as shown in Figure 8 (grey circles). While only 5% GNR-collagen nanocomposites were used in this work, future work could include optimizing the nanocomposites to minimize the amount of GNRs used while still maintaining reasonably low and inexpensive laser power densities to produce sufficient heat for soldering. In Figure 8 unlike Figure 5, a thermocouple has not been placed below the tissue surface, and it can be seen that the temperature variations are much less extreme.

From Figure 9, we can see that the laser soldering condition that results in a temperature of 57°C results in a 21.9% return in tissue tensile strength that is not statistically significant compared to the tensile strength of ruptured intestine. By contrast, the soldering condition that results in a temperature of 75°C results in a 58.5% return in tensile strength of that of the native tissue compared to the ruptured tissue. The effect of these two temperatures is even more pronounced in the comparison of the fluid pressures at which intestine rupture first occurs. When LTS is performed at 57°C for 4 minutes, there is a small 4.8% increase return in the native tissue pressure, which is statistically insignificant from the unsoldered ruptured intestine and thus has remained largely unsoldered. By comparison, soldering at the 75°C condition for 4 minutes results in a 46.9% return in rupture pressure of the native intestine, which is significantly different than that of the untreated ruptured tissue and a strong indication of successful soldering. Because the improvement in rupture pressure is nearly 10 fold in the 75°C treatment compared to the 57°C treatment, we can reasonably assume that the 57°C did not reach or maintain the critical soldering temperature for sufficient treatment time, while the 75°C treatment did elicit tissue fusion. These results strongly advocate for a correlation between soldering temperature and closure strength. The temperature predictions from Figure 6 suggest that there is sufficient heat to induce soldering in the full thickness of the 4 mm intestine with a critical soldering temperature of 60°C. Also, due to the highly localized predicted elevated temperatures, sealing of peripheral tissue or inadvertently sealing the intestinal lumen closed appears highly unlikely. Further work using this spatiotemporal model to predict solder strengths based on LTS temperatures will incorporate the fundamental investigation of the heat-induced chemical mechanisms involved in tissue fusion.

Mouse Cadaver Colon Model

The mathematical model of temperature distribution in the LTS patch and mouse intestine predicted a maximum temperature of approximately 48°C over the 4 minutes of laser duration (Figure 10). As with the porcine predictions, the maximum temperature was attained near the center of the elliptical region directly exposed to the laser. The region of elevated temperatures extended outward approximately 3 mm past the outer edge of the patch in both the positive and negative x-directions, but the magnitude of the temperature elevation was very small for most of the tissue surrounding the patch. The temperature outside of the patch region reached a high of approximately 32°C (Figure 10).

Temperatures were recorded at three different points within the tissue below the patch: inside the primary lumen, between the primary and secondary lumen, and inside the secondary lumen (Figure 2). The thickness of the intestinal wall was assumed to be approximately 0.5 mm thick, meaning the temperatures were recorded at depths of 0.5 mm, 1.0 mm, and 1.5 mm below the surface of the intestine (i.e., below the patch). The experimentally measured temperatures at each location are plotted versus time for the duration of the laser treatment, and compared with the mathematical model predictions of temperature at the same locations in Figure 11.

The model predictions (shown as lines in Figure 11) show many of the same characteristics observed in the experimental data (shown as distinct points). Specifically, the rate at which the temperature increases within the tissue is similar between the model and experiment, and the temperature differences between the tissue layers is also consistent. It should be noted that for the upper most location (thermocouple in Figure 2B), the laser was turned off after 2 minutes so comparisons with the model predictions after that time are not possible. There are also some differences between the model predictions and experimental measurements, especially early in the experiment between 30 seconds and one minute. These differences could stem from the location of the probes in the model relative to the actual location from the experiment because the exact thickness of the intestine wall is not known. Similarly, they could be caused by the thermocouple directly absorbing some laser energy. These results suggest that the heat generated in LTS is not sufficient to seal adjacent tissue inadvertently.

Conclusions

A spatiotemporal model has been developed for predicting temperature changes and potential thermal damage during the LTS process with the long-term goal of enabling optimized outcomes and reducing total experimental work by correlating laser power density and treatment duration to solder strength. The model predicts temperature within a photothermal nanocomposite material and surrounding tissue as well as cell death in tissue during the LTS process. For the model results replicating the porcine experimental measurements, the surface of the composite patch reaches temperatures in excess of 60°C while the adjacent tissue directly below the nanocomposite reaches temperatures in excess of 50°C. However, the elevated tissue temperatures are only reached for the few minutes the laser remains on, and temperatures return to normal within a few minutes of the laser being turned off. All temperature predictions from the mathematical model are consistent with experimental measurements. The model predicts that a high fraction of cells are killed by

hyperthermia in the tissue immediately adjacent to the nanocomposite, but this is a relatively small region that in a surgical setting would contain negative space and tissue subject to cell death already because of the incision, and the vast majority of cells are expected to survive just a short distance (~2 mm) from the patch. The mathematical model was also assessed through comparisons to temperature measurements from LTS experiments on mouse intestines. In this case, temperature measurements at multiple tissue depths were available, and the mathematical model predictions were quantitatively consistent with the experimental measurements.

Future work will focus on predicting the strength of the solder and identifying conditions that minimize cell death and necrosis in the region adjacent to the patch. Future work also will include mechanistic work with in vivo data to better understand the molecular processes involved in tissue fusion and incorporate these into a predictive model. In addition to laser power density and duration of irradiation, a number of treatment parameters can be varied in order to optimize LTS using photothermal nanocomposites. These include concentration of the chromophore GNRs in the nanocomposite, laser power density, duration of exposure, humidity, blood flow, and tissue homogeneity. Future work on this mathematical model includes incorporating more variables into a predictive model that will assist in the identification of optimal conditions for tissue fusion and repair.

Acknowledgments

References

1. Tajirian AL, Goldberg DJ. A review of sutures and other skin closure materials. J Cosmet Laser Ther. 2010; 12(6):296–302. [PubMed: 21142740]

2. Lauto A, Mawad D, Foster LJR. Adhesive biomaterials for tissue reconstruction. Journal of Chemical Technology & Biotechnology. 2008; 83(4):464–472.

3. Huang HC, Walker CR, Nanda A, Rege K. Laser Welding of Ruptured Intestinal Tissue Using Plasmonic Polypeptide Nanocomposite Solders. Acs Nano. 2013; 7(4):2988–2998. [PubMed: 23530530]

4. Hyman N, Manchester TL, Osler T, Burns B, Cataldo PA. Anastomotic leaks after intestinal anastomosis - It's later than you think. Annals of Surgery. 2007; 245(2):254–258. [PubMed: 17245179]

5. Park IJ. Influence of Anastomotic Leakage on Oncological Outcome in Patients with Rectal Cancer. J Gastrointest Surg. 2010; 14(7):1190–1196. [PubMed: 20094811]

6. Komatsu F, Mori R, Uchio Y. Optimum surgical suture material and methods to obtain high tensile strength at knots: problems of conventional knots and the reinforcement effect of adhesive agent. J Orthop Sci. 2006; 11(1):70–74. [PubMed: 16437352]

7. Bleier BS, Cohen NM, Bloom JD, Palmer JN, Cohen NA. Laser tissue welding in lung and tracheobronchial repair: an animal model. Chest. 2010; 138(2):345–349. [PubMed: 20299627]

8. Duarte AP, Coelho JF, Bordado JC, Cidade MT, Gil MH. Surgical adhesives: Systematic review of the main types and development forecast. Progress in Polymer Science. 2012; 37(8):1031–1050.

9. Rose S, Prevoteau A, Elziere P, Hourdet D, Marcellan A, Leibler L. Nanoparticle solutions as adhesives for gels and biological tissues. Nature. 2014; 505(7483):382. [PubMed: 24336207]

10. Meddahi-Pelle A, Legrand A, Marcellan A, Louedec L, Letourneur D, Leibler L. Organ Repair, Hemostasis, and In Vivo Bonding of Medical Devices by Aqueous Solutions of Nanoparticles. Angew Chem Int Edit. 2014; 53(25):6369–6373.

11. Foyt D, Johnson JP, Kirsch AJ, Bruce JN, Wazen JJ. Dural closure with laser tissue welding. Otolaryngol Head Neck Surg. 1996; 115(6):513–518. [PubMed: 8969756]

12. Bleier BS, Palmer JN, Sparano AM, Cohen NA. Laser-assisted cerebrospinal fluid leak repair: an animal model to test feasibility. Otolaryngol Head Neck Surg. 2007; 137(5):810–814. [PubMed: 17967651]

13. Barak A, Eyal O, Rosner M, Belotserkousky E, Solomon A, Belkin M, Katzir A. Temperature-controlled CO2 laser tissue welding of ocular tissues. Surv Ophthalmol. 1997; 42:S77–S81. [PubMed: 9603292]

14. Nakadate R, Omori S, Ikeda T, Akahoshi T, Ogui S, Arata J, Onogi S, Hashizume M. Improving the strength of sutureless laser-assisted vessel repair using preloaded longitudinal compression on tissue edge. Lasers Surg Med. 2017; 49(5):533–538. [PubMed: 28129436]

15. Matteini P, Ratto F, Rossi F, Pini R. Emerging concepts of laser-activated nanoparticles for tissue bonding. J Biomed Opt. 2012; 17(1):010701. [PubMed: 22352632]

16. Rossi F, Pini R, Menabuoni L, Mencucci R, Menchini U, Ambrosini S, Vannelli G. Experimental study on the healing process following laser welding of the cornea. J Biomed Opt. 2005; 10(2): 024004. [PubMed: 15910078]

17. Ratto F, Matteini P, Rossi F, Menabuoni L, Tiwari N, Kulkarni SK, Pini R. Photothermal effects in connective tissues mediated by laser-activated gold nanorods. Nanomedicine. 2009; 5(2):143–151. [PubMed: 19223241]

18. Matteini P, Sbrana F, Tiribilli B, Pini R. Atomic force microscopy and transmission electron microscopy analyses of low-temperature laser welding of the cornea. Lasers Med Sci. 2009; 24(4): 667–671. [PubMed: 18982404]

19. Kelkar SS, McCabe-Lankford E, Albright R, Harrington P, Levi-Polyachenko NH. Dual wavelength stimulation of polymeric nanoparticles for photothermal therapy. Lasers Surg Med. 2016; 48(9):893–902. [PubMed: 27636556]

20. Urie R, Quraishi S, Jaffe M, Rege K. Gold Nanorod-Collagen Nanocomposites as Photothermal Nanosolders for Laser Welding of Ruptured Porcine Intestines. ACS Biomaterials Science & Engineering. 2015; 1(9):805–815.

21. Schonfeld A, Kabra ZM, Constantinescu M, Bosshardt D, Stoffel MH, Peters K, Frenz M. Binding of indocyanine green in polycaprolactone fibers using blend electrospinning for in vivo laser-assisted vascular anastomosis. Lasers Surg Med. 2017

22. Hoffman GT, Byrd BD, Soller EC, Heintzelman DL, McNally-Heintzelman KM. Alternative chromophores for use in light-activated surgical adhesives: optimization of parameters for tensile strength and thermal damage profile. International Society for Optics and Photonics. 2003:174–181.

23. Bleustein CB, Walker CN, Felsen D, Poppas DP. Semi-solid albumin solder improved mechanical properties for laser tissue welding. Lasers Surg Med. 2000; 27(2):140–146. [PubMed: 10960820]

24. Garcia P, Mines MJ, Bower KS, Hill J, Menon J, Tremblay E, Smith B. Robotic laser tissue welding of sclera using chitosan films. Lasers Surg Med. 2009; 41(1):60–67. [PubMed: 19143017]

25. Hoffman, Byrd, Soller. Alternative chromophores for use in light-activated surgical adhesives: optimization of parameters for tensile strength and thermal damage profile. International Society for Optics and Photonics. 2003

26. Lewinski N, Colvin V, Drezek R. Cytotoxicity of nanoparticles. Small. 2008; 4(1):26–49. [PubMed: 18165959]

27. Almeida JPM, Chen AL, Foster A, Drezek R. In vivo biodistribution of nanoparticles. Nanomedicine-Uk. 2011; 6(5):815–835.

28. Huang HC, Rege K, Heys JJ. Spatiotemporal Temperature Distribution and Cancer Cell Death in Response to Extracellular Hyperthermia Induced by Gold Nanorods. Acs Nano. 2010; 4(5):2892–2900. [PubMed: 20387828]

29. Huang HC, Nanda A, Rege K. Investigation of Phase Separation Behavior and Formation of Plasmonic Nanocomposites from Polypeptide-Gold Nanorod Nanoassemblies. Langmuir. 2012; 28(16):6645–6655. [PubMed: 22394160]

30. Schober R, Ulrich F, Sander T, Durselen H, Hessel S. Laser-Induced Alteration of Collagen Substructure Allows Microsurgical Tissue Welding. Science. 1986; 232(4756):1421–1422. [PubMed: 3715454]

31. Bass LS, Moazami N, Pocsidio J, Oz MC, Logerfo P, Treat MR. Changes in Type-I Collagen Following Laser-Welding. Lasers in Surgery and Medicine. 1992; 12(5):500–505. [PubMed: 1406002]

32. Matteini P, Cicchi R, Ratto F, Kapsokalyvas D, Rossi F, de Angelis M, Pavone FS, Pini R. Thermal transitions of fibrillar collagen unveiled by second-harmonic generation microscopy of corneal stroma. Biophys J. 2012; 103(6):1179–1187. [PubMed: 22995490]

33. Jacques SL, Prahl SA. Modeling Optical and Thermal Distributions in Tissue during Laser Irradiation. Lasers in Surgery and Medicine. 1987; 6(6):494–503. [PubMed: 3573921]

34. Matteini P, Sbrana F, Tiribilli B, Pini R. Atomic force microscopy and transmission electron microscopy analyses of low-temperature laser welding of the cornea. Lasers in Medical Science. 2009; 24(4):667–671. [PubMed: 18982404]

35. Matteini P, Ratto F, Rossi F, Cicchi R, Stringari C, Kapsokalyvas D, Pavone FS, Pini R. Photothermally-induced disordered patterns of corneal collagen revealed by SHG imaging. Opt Express. 2009; 17(6):4868–4878. [PubMed: 19293918]

36. He WP, Frueh J, Shao JX, Gai MY, Hu N, He Q. Guidable GNR-Fe3O4-PEM@SiO2 composite particles containing near infrared active nanocalorifiers for laser assisted tissue welding. Colloid Surface A. 2016; 511:73–81.

37. He WP, Frueh J, Hu N, Liu LP, Gai MY, He Q. Guidable Thermophoretic Janus Micromotors Containing Gold Nanocolorifiers for Infrared Laser Assisted Tissue Welding. Adv Sci. 2016; 3(12)

38. Huang HC, Koria P, Parker SM, Selby L, Megeed Z, Rege K. Optically Responsive Gold Nanorod-Polypeptide Assemblies. Langmuir. 2008; 24(24):14139–14144. [PubMed: 19360961]

39. Nikoobakht B, El-Sayed MA. Preparation and growth mechanism of gold nanorods (NRs) using seed-mediated growth method. Chem Mater. 2003; 15(10):1957–1962.

40. Shao JX, Xuan MJ, Dai LR, Si TY, Li JB, He Q. Near-Infrared-Activated Nanocalorifiers in Microcapsules: Vapor Bubble Generation for In Vivo Enhanced Cancer Therapy. Angew Chem Int Edit. 2015; 54(43):12782–12787.

41. Xuan MJ, Wu ZG, Shao JX, Dai LR, Si TY, He O. Near Infrared Light-Powered Janus Mesoporous Silica Nanoparticle Motors. J Am Chem Soc. 2016; 138(20):6492–6497. [PubMed: 27152728]

42. Ruijgrok PV, Verhart NR, Zijlstra P, Tchebotareva AL, Orrit M. Brownian Fluctuations and Heating of an Optically Aligned Gold Nanorod. Physical Review Letters. 2011; 107(3)

43. Jauffred L, Taheri SMR, Schmitt R, Linke H, Oddershede LB. Optical Trapping of Gold Nanoparticles in Air. Nano Lett. 2015; 15(7):4713–4719. [PubMed: 26083715]

44. Pennes HH. Analysis of Tissue and Arterial Blood Temperatures in the Resting Human Forearm. Journal of Applied Physiology. 1948; 1(2):93–122. [PubMed: 18887578]

45. Fuentes D, Oden JT, Diller KR, Hazle JD, Elliott A, Shetty A, Stafford RJ. Computational Modeling and Real-Time Control of Patient-Specific Laser Treatment of Cancer. Annals of Biomedical Engineering. 2009; 37(4):763–782. [PubMed: 19148754]

46. Kim BM, Jacques SL, Rastegar S, Thomsen S, Motamedi M. Nonlinear finite-element analysis of the role of dynamic changes in blood perfusion and optical properties in laser coagulation of tissue. Ieee Journal of Selected Topics in Quantum Electronics. 1996; 2(4):922–933.

47. Rylander MN, Feng Y, Bass J, Diller KR. Heat shock protein expression and injury optimization for laser therapy design. Lasers Surg Med. 2007; 39(9):731–746. [PubMed: 17960756]

48. Diller KR, Valvano JW, Pearce JA. Bioheat transfer. CRC handbook of thermal engineering. 2000; 4:114–215.

49. Rylander MN, Feng Y, Bass J, Diller KR. Heat shock protein expression and injury optimization for laser therapy design. Lasers in Surgery and Medicine. 2007; 39(9):731–746. [PubMed: 17960756]

50. Henriques FC. Studies of Thermal Injury .5. The Predictability and the Significance of Thermally Induced Rate Processes Leading to Irreversible Epidermal Injury. Arch Pathol. 1947; 43(5):489–502.

51. Bhowmick P, Coad JE, Bhowmick S, Pryor JL, Larson T, De la Rosette J, Bischof JC. In vitro assessment of the efficacy of thermal therapy in human benign prostatic hyperplasia. International Journal of Hyperthermia. 2004; 20(4):421–439. [PubMed: 15204522]

52. Lepock JR. Cellular effects of hyperthermia: relevance to the minimum dose for thermal damage. International Journal of Hyperthermia. 2003; 19(3):252–266. [PubMed: 12745971]

53. Pearce, J., Thomsen, S. Optical-thermal response of laser-irradiated tissue. Springer; 1995. Rate process analysis of thermal damage; p. 561-606.

54. Dewhirst MW, Viglianti BL, Lora-Michiels M, Hanson M, Hoopes PJ. Basic principles of thermal dosimetry and thermal thresholds for tissue damage from hyperthermia. International Journal of Hyperthermia. 2003; 19(3):267–294. [PubMed: 12745972]

55. Constantinescu MA, Alfieri A, Mihalache G, Stuker F, Ducray A, Seiler RW, Frenz M, Reinert M. Effect of laser soldering irradiation on covalent bonds of pure collagen. Lasers Med Sci. 2007; 22(1):10–14. [PubMed: 17115238]

56. Sriramoju V, Savage H, Katz A, Muthukattil R, Alfano RR. Management of heat in laser tissue welding using NIR cover window material. Lasers Surg Med. 2011; 43(10):991–997. [PubMed: 22127755]

57. Matteini P, Rossi F, Menabuoni L, Pini R. Microscopic characterization of collagen modifications induced by low-temperature diode-laser welding of corneal tissue. Lasers Surg Med. 2007; 39(7):597–604. [PubMed: 17868101]
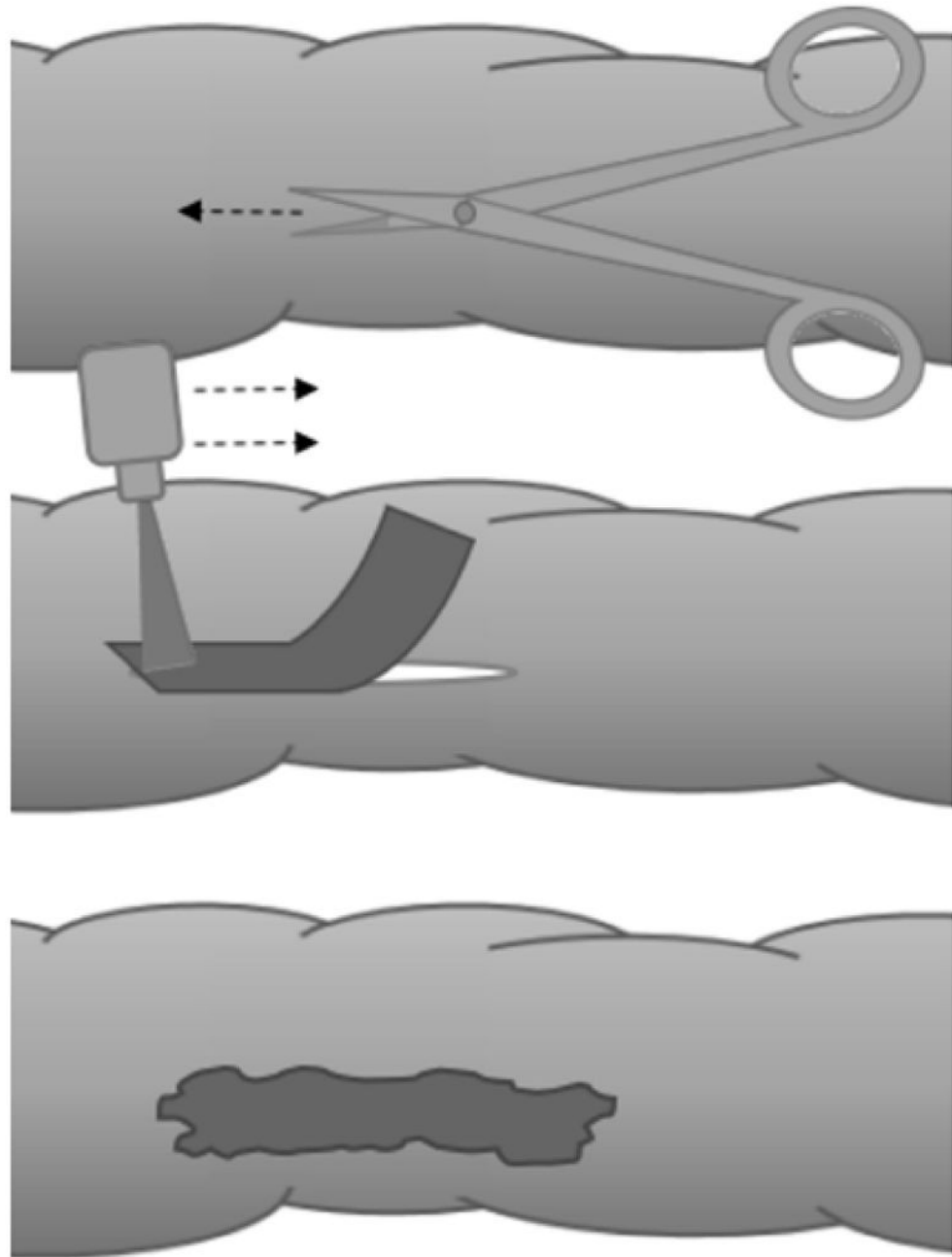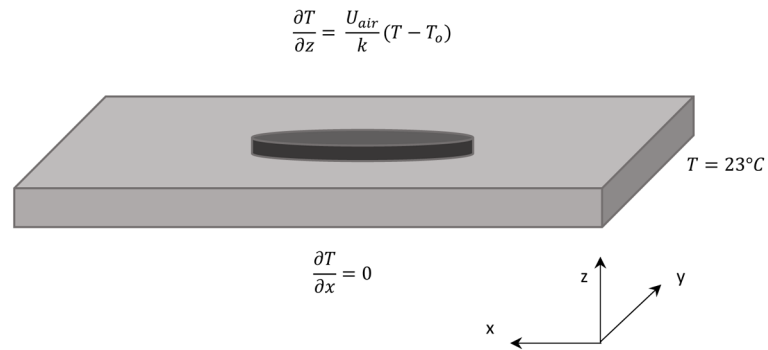
FIGURE 1.
A SCHEMATIC SHOWING THE INCISION OF COLON TISSUE (TOP) AFTER WHICH
THE INCISION IS CLOSED USING A PHOTORESPONSIVE NANOCOMPOSITE
PATCH (CENTER) AND LASER IRRADIATION TO CREATE A RAPID, ROBUST
SEAL (BOTTOM) THROUGH LASER TISSUE SOLDERING.
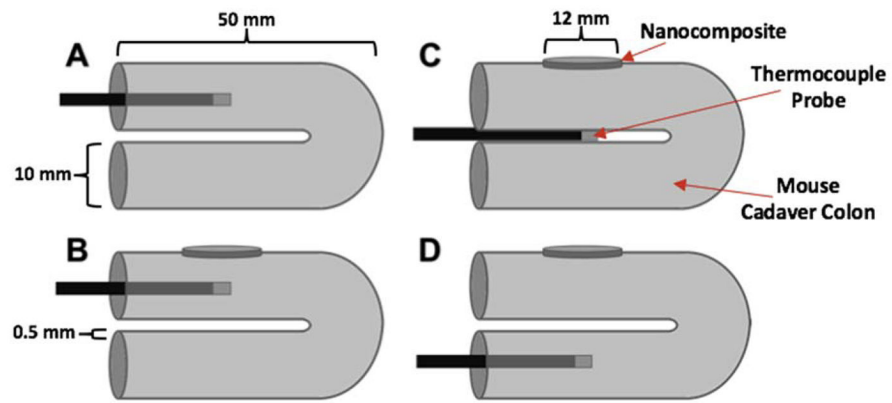
FIGURE 2.
A SCHEMATIC DEPICTING THE NANOCOMPOSITE PATCH AND THREE
DIFFERENT TEMPERATURE PROBE LOCATIONS WITHIN THE MOUSE CADAVER
COLON USED FOR COMPARISON TO THE MATHEMATICAL MODEL
PREDICTIONS.

$$\frac{\partial T}{\partial z} = \frac{U_{air}}{k}(T - T_o)$$

$$T = 23°C$$

$$\frac{\partial T}{\partial x} = 0$$

FIGURE 3.
THE BASIC SHAPE OF THE MATHEMATICAL MODEL DOMAIN REPRESENTING THE FLATTENED INTESTINE (LIGHT GREY) WITH DIMENSIONS OF [50MM × 20MM × 4 MM] AND A CIRCULAR PATCH (DARK GREY) OF 10 MM DIAMETER PROTRUDING ATOP THE CENTER OF THE BRICK WAS USED IN THE MODEL WITH ITS CORRESPONDING BOUNDARY.
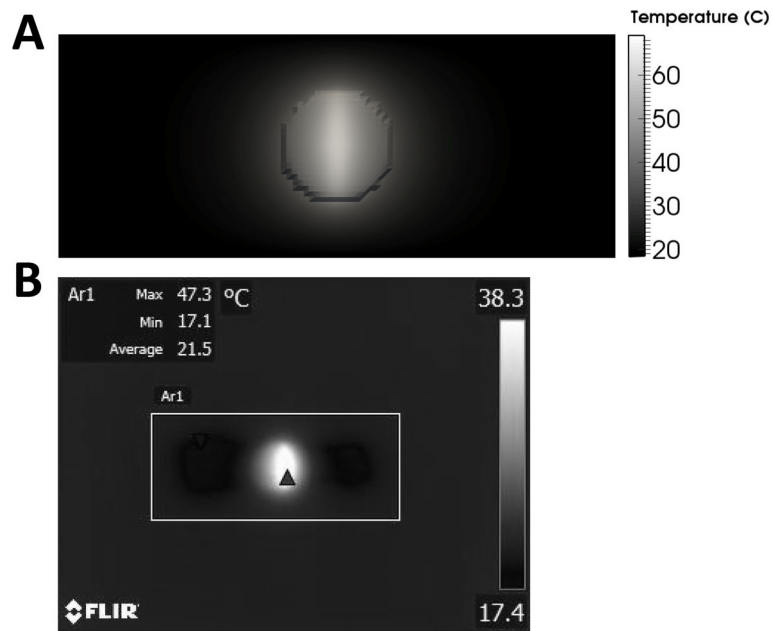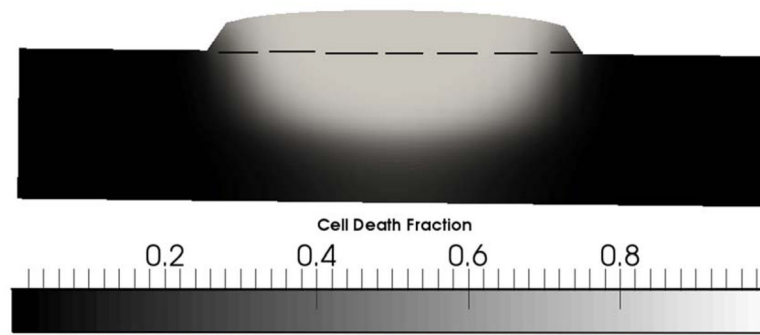
Figure 4.
(A) Surface temperature prediction from the heat transfer model after 4 minutes of laser treatment at 2.33 W/cm^2 CW in porcine intestine, and (B) experimental measurement of the surface temperature measurement of the porcine intestine (box) after a similar time period.
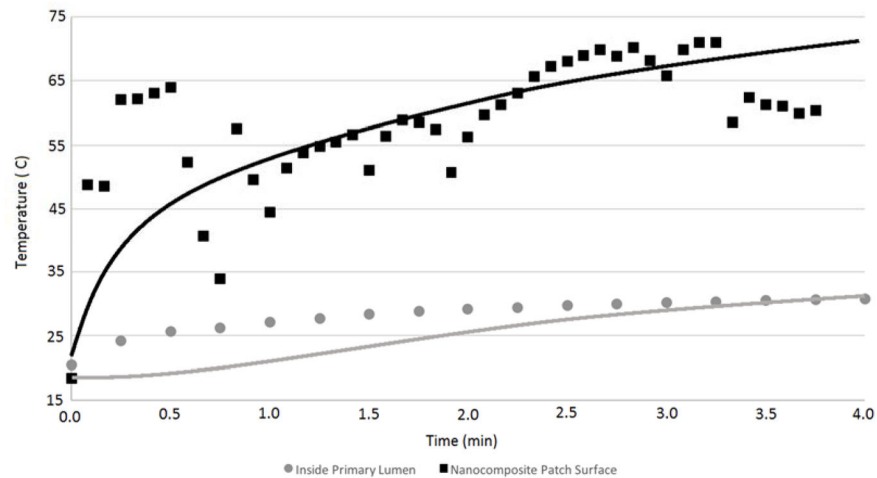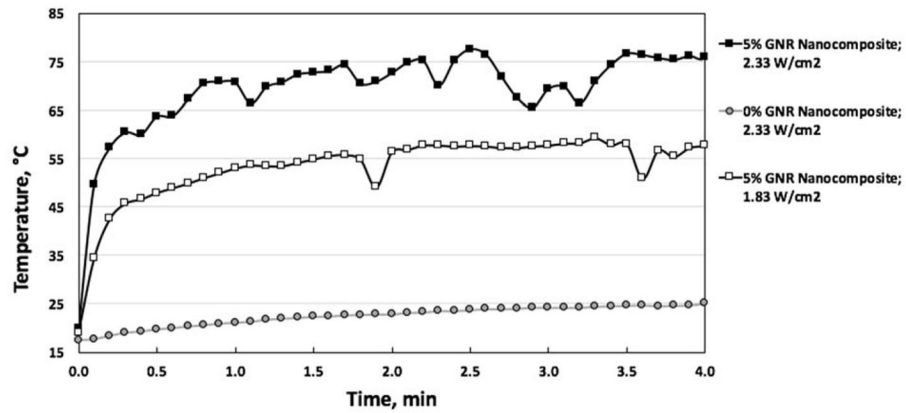
FIGURE 5.
EXPERIMENTAL PORCINE TEMPERATURE DATA IN COMPARISON WITH THE
MODEL PREDICTION OF TEMPERATURE. THE SOLID LINES (UPPER AND
LOWER) REPRESENT THE MODEL TEMPERATURE PREDICTION AT TWO
DIFFERENT LOCATIONS (SURFACE TEMPERATURES AND INSIDE THE PRIMARY
LUMEN) CORRESPONDING TO THE SAME LOCATIONS AS THE EXPERIMENTAL
MEASUREMENTS. EXPERIMENTAL DATA ARE REPRESENTATIVE OF N=3
INDEPENDENT EXPERIMENTS.

FIGURE 6.
PROFILE VIEW OF THE TEMPERATURE GRADIENT THROUGH THE X–Z PLANE. THE DASHED LINE (–) REPRESENTS THE PATCH-TISSUE INTERFACE, WITH THE AREA ABOVE ENCOMPASSING THE PATCH AND THE AREA BELOW ENCOMPASSING THE TISSUE.

FIGURE 7.
CELL DEATH FRACTION THROUGH THE PORCINE TISSUE AFTER 4 MINUTES OF LASER TREATMENT AT 2.33 W/CM^2 CW. THE DASHED LINE (–) REPRESENTS THE PATCH-TISSUE INTERFACE, WITH THE AREA ABOVE ENCOMPASSING THE CELL-FREE PATCH AND THE AREA BELOW ENCOMPASSING THE TISSUE.

FIGURE 8.
NANOCOMPOSITE SURFACE TEMPERATURE DURING LASER SOLDERING OF PORCINE INTESTINE AS MEASURED BY IR IMAGES. GREY CIRCLES INDICATE COLLAGEN PATCHES WITH 0% GNRs IRRADIATED AT 2.33 W/CM^2, WHITE BOXES REPRESENT 5% GNR-COLLAGEN NANOCOMPOSITES IRRADIATED AT 1.83 W/CM^2, AND BLACK BOXES SHOW 5% GNR-COLLAGEN NANOCOMPOSITES IRRADIATED AT 2.33 W/CM^2. CURVES ARE REPRESENTATIVE OF THE TEMPERATURES REACHED IN N=3 INDEPENDENT EXPERIMENTS AND THE LINES CONNECTING THE DATA ARE ONLY FOR VISUALIZATION OF DATA TRENDS.
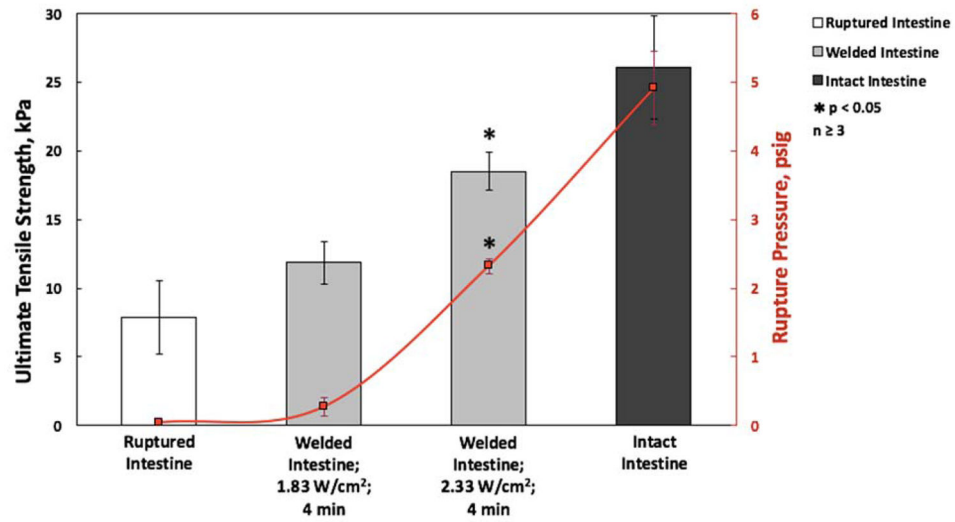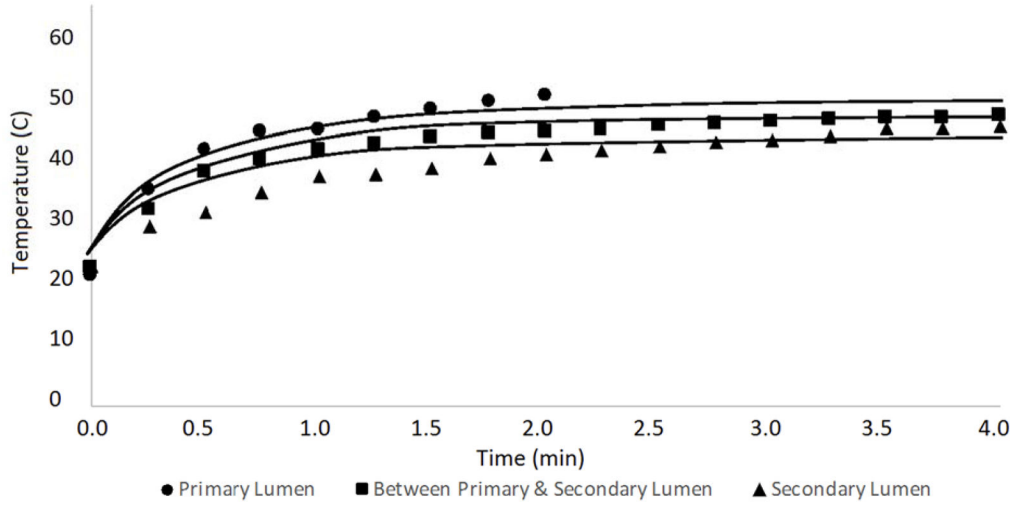
FIGURE 9.
ULTIMATE TENSILE STRENGTH AND RUPTURE PRESSURE OF PORCINE INTESTINE. SOLDERED INTESTINES (GREY COLUMNS) WERE LASER SOLDERED USING 5% GNR-COLLAGEN NANOCOMPOSITES AS 1.83 OR 2.33 W/CM^2 FOR 4 MINUTES AND ARE COMPARED TO RUPTURED INTESTINE (WHITE COLUMN) AND INTACT INTESTINE (BLACK COLUMN). ALSO, THE RED LINE INDICATES THE RUPTURE PRESSURE OF INTESTINE IN THESE CONDITIONS.

FIGURE 10.
SURFACE TEMPERATURE PREDICTION FOR THE HEAT TRANSFER MODEL FOR
MOUSE TISSUE AFTER 4 MINUTES OF LASER DURATION.

FIGURE 11.
TEMPERATURE VERSUS TIME CURVE FOR THE VARIOUS THERMOCOUPLE
LOCATIONS SHOWN IN FIGURE 2 IN THE MOUSE INTESTINAL TISSUE
(DISCRETE POINTS), AND THE SOLID LINES REPRESENT THE MODEL
PREDICTION FOR EACH RESPECTIVE LOCATION. THE LOWEST LINE
CORRESPONDS TO WITHIN THE SECONDARY LUMEN, THE MIDDLE LINE
SIGNIFIES THE TEMPERATURE BETWEEN THE PRIMARY AND SECONDARY
LUMEN, AND THE TOP-MOST LINE CORRESPONDS TO WITHIN THE PRIMARY
LUMEN.

TABLE 1

HEAT TRANSFER AND NANOCOMPOSITE PATCH PARAMETERS USED IN THE MATHEMATICAL MODEL BASED ON REFERENCES [28,47,48]

Parameter	Variable	Value
Optical Density	OD	0.1
Density	ρ	$0.001\frac{g}{mm^3}$
Heat Capacity	C_p	$3.4\frac{J}{g\cdot K}$
Thermal Conductivity	k	$0.58\frac{W}{m\cdot K}$
Overall Heat Transfer Coefficient (air)	U_{air}	$0.08\frac{W}{m^2\cdot K}$
Laser Power Density (area)	Q	$0.0233\frac{W}{mm^2}$
Optical Thickness	d	$0.50\ mm$
Laser Power Density (volume)	Q_{laser}	$0.0466\frac{W}{mm^3}$
Overall Laser Expression	$Q_{expression}$	$13.7\frac{K}{s}$
Thermal Diffusivity	a	$0.171\frac{mm^2}{s}$
Initial Temperature	T_0	$23\ ^{\circ}C$
Universal Gas Constant	R	$0.008314\frac{kJ}{mol\cdot K}$
Arrhenius Scaling Factor	A	$6\times10^{29}\ S^{-1}$
Arrhenius Activation Energy	E_a	$200\frac{kJ}{mol}$